Electronic Supplementary Material (ESI) for Journal of Materials Chemistry A.

SUPPORTING INFORMATION

Pure hydrogen and sulfur production from H_2S by electrochemical approach using NiCu-MoS_2 catalyst

Mukesh Kumar and Tharamani C. Nagaiah *

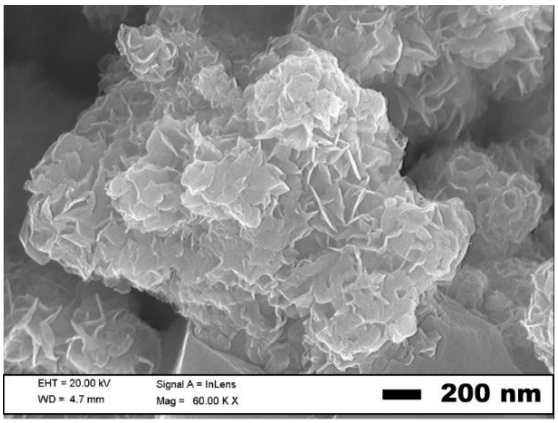

Fig. S1. (a) FE-SEM images of MoS_2.

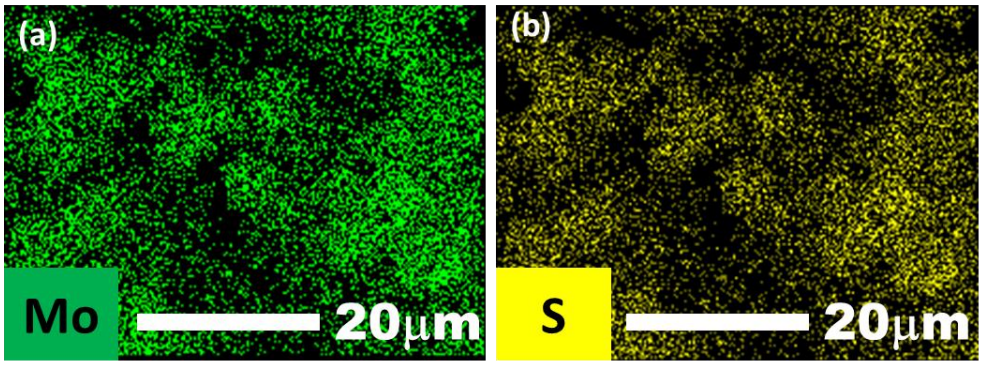

Fig. S2. Elemental dot mapping images representing the distribution of (a) Mo and (b) S of MoS_2.

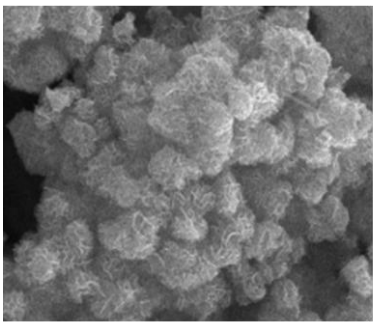

Elements	Atomic Percentage
S K	61.01
Ni K	4.28
Cu K	4.22
Mo L	30.51

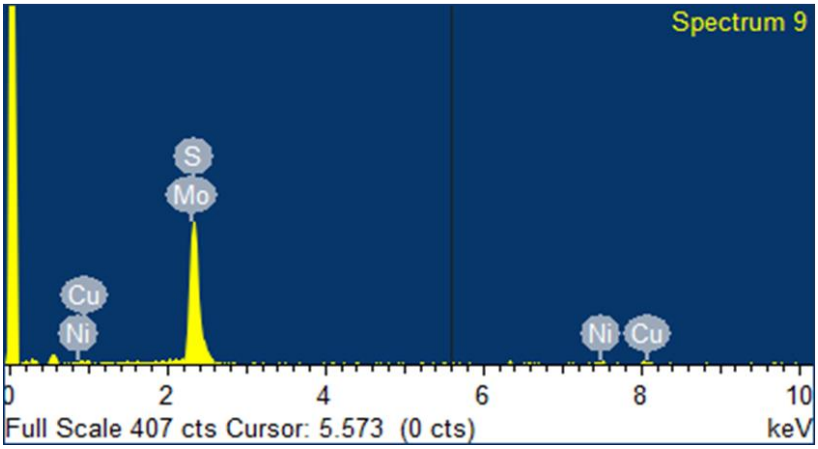

Fig. S3. SEM image and corresponding EDX spectrum of NiCu-MoS_2 along with composition.

These results are well supported by the combined MP-AES and CHNS studies. The composition of Ni, Cu and Mo is determined from MP-AES and S was determined by CHNS and listed in Table S1.

Table S1: MP-AES and CHNS results of NiCu-MoS_2.

Elements	Weight percentage	Atomic percentage
Ni	4.85	4.83
Cu	4.75	4.76
Mo	55.35	31.5
S (CHNS)	35.05	58.91

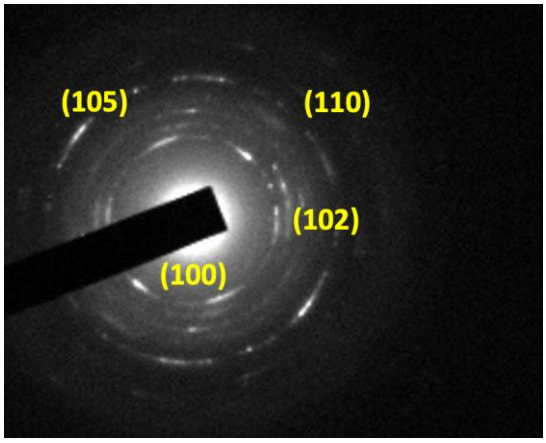

Fig. S4. SAED pattern of Ni-Cu-MoS_2.

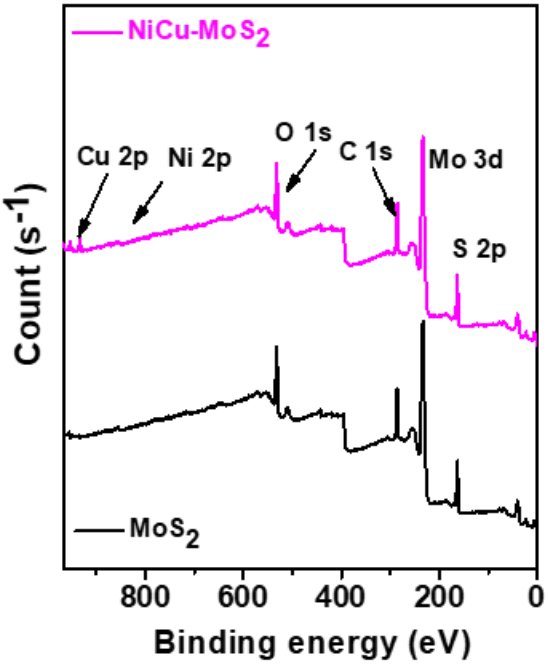

Fig. S5. (a) Comparative XPS survey spectra of MoS_2 and NiCu-MoS_2.

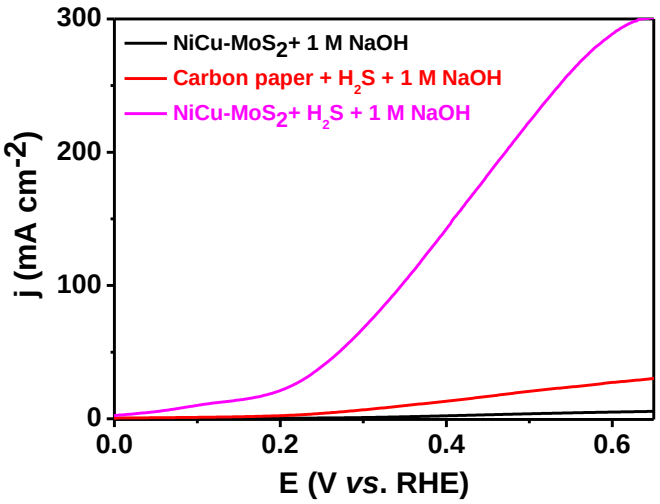

Fig. S6. Linear sweep voltammograms demonstrating SOR activity under various conditions in H_2S saturated 1 M NaOH electrolyte at a scan rate of 5 mV s^{-1}, CE: graphite rod, RE: Hg/HgO/1 M NaOH.

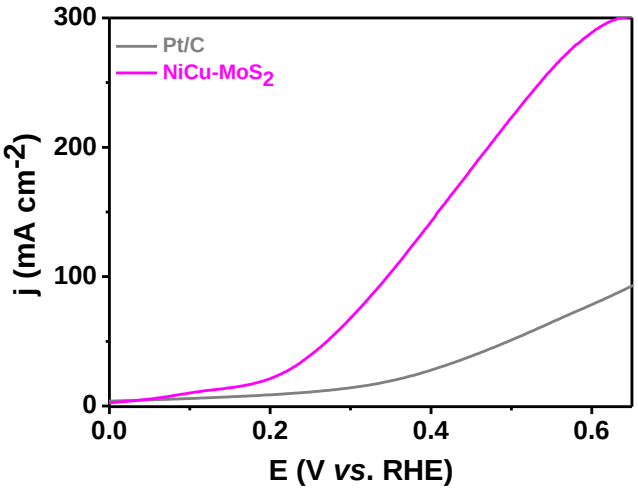

Fig. S7. Linear sweep voltammograms demonstrating SOR activity of Pt/C and NiCu-MoS_2 in H_2S saturated 1 M NaOH electrolyte at a scan rate of 5 mV s^{-1}, CE: graphite rod, RE: Hg/HgO/1 M NaOH.

Electrochemical surface area (ECSA):

To uncover the superior performance of the catalyst towards SOR, ECSA is a vital tool that directly influences catalyst performance due to its close relationship with the no. of active sites. ECSA was calculated from double-layer capacitance C_{dl}, for that initially CVs were recorded at various scan rates

ranging from 5-400 mV s^{-1} in the non-faradaic region from 0.0 V to 0.1 V *vs.* RHE in H_2S saturated 1 M NaOH. The plot of the average current density ($(I_a+I_c)/2$) *vs.* scan rates gives us the double-layer capacitance. ECSA is calculated by dividing this slope with specific capacitance (20-60 μF cm^{-2}) of the flat standard surface in the present study its value is considered to be 40 μF cm^{-2}. [1] The obtained results indicate that ECSA was drastically enhanced for NiCu-MoS_2 catalysts. The ECSA for NiCu-MoS_2 is 8.14 $cm^{2,}$ higher than all other catalysts (detailed in Table S2).

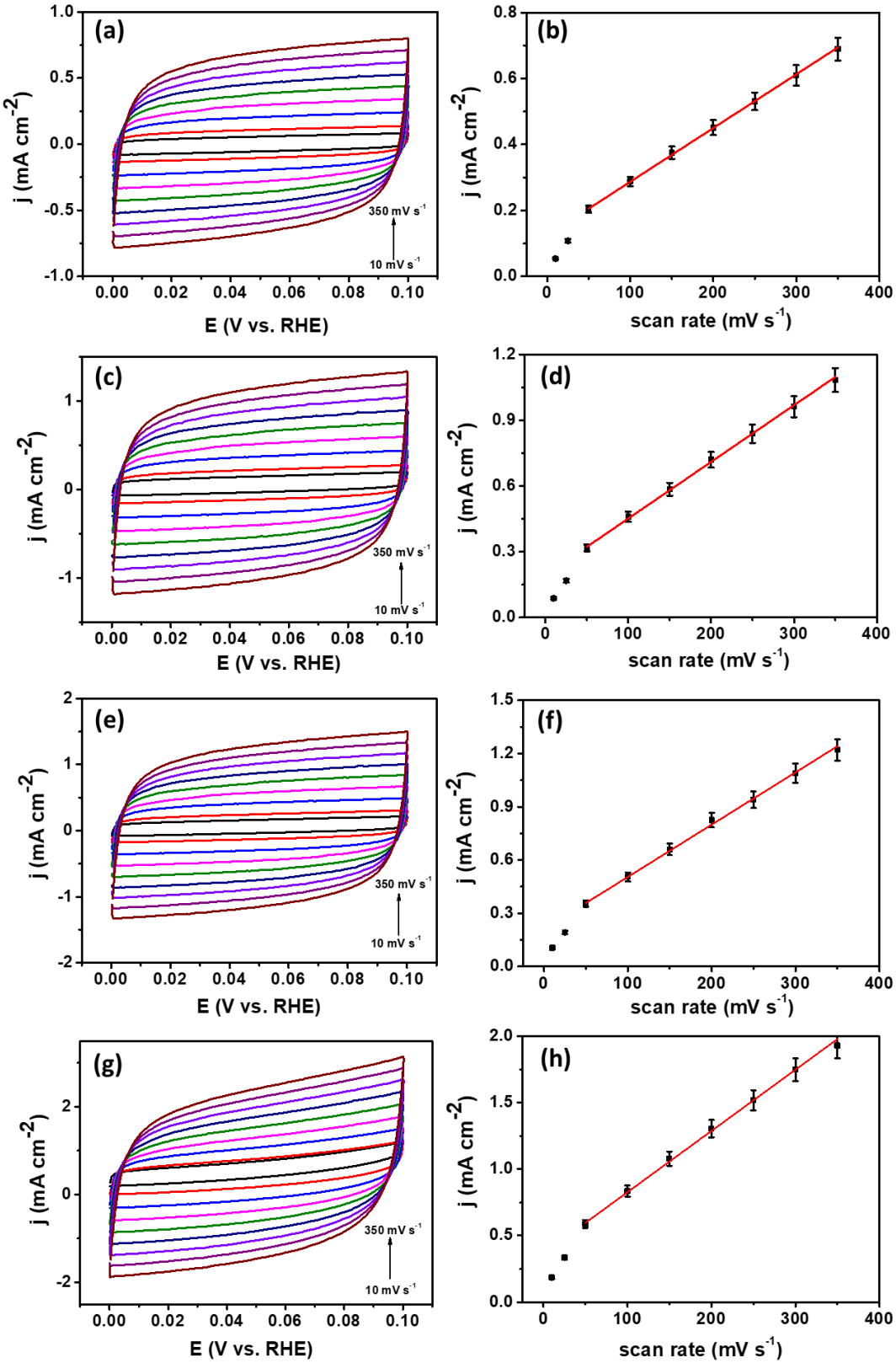

Fig. S8. Cyclic voltammograms of (a) MoS_2, (c) Cu-MoS_2, (e) Ni-MoS_2, (g) NiCu-MoS_2 at various scan rates in the non-faradaic potential region and (b), (d), (f), (h), are corresponding average current versus scan rates plot in H_2S saturated 1 M NaOH, CE: graphite rod, RE: Hg/HgO/1 M NaOH.

Table S2: Electrochemical surface area (ECSA) of various catalysts.

Catalysts	ECSA (cm^2) at 0.050 V *vs.* RHE
MoS_2	2.88
Cu-MoS_2	4.56
Ni-MoS_2	5.21
NiCu-MoS_2	8.148

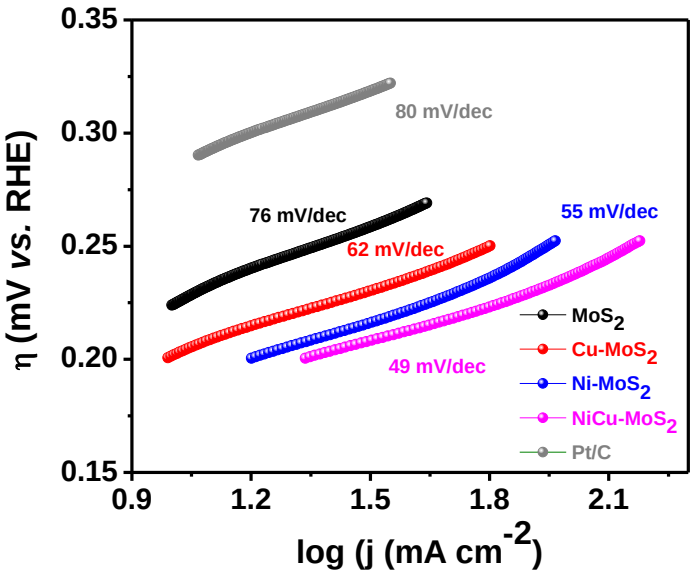

Fig. S9. Tafel plots for various catalysts extracted from Fig. 2a (main manuscript) in H_2S saturated 1 M NaOH electrolyte, CE: graphite rod, RE: Hg/HgO/1 M NaOH.

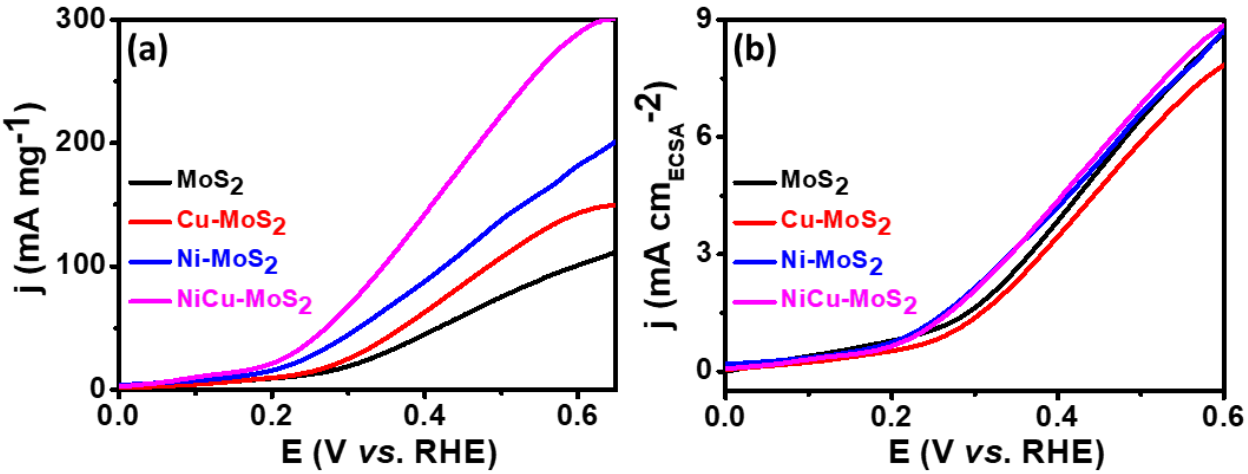

Fig. S10 (a) Linear sweep voltammograms of various catalysts at a scan rate of 5 mV s^{-1} in terms of (a) mass specific and (b) ECSA specific SOR activity.

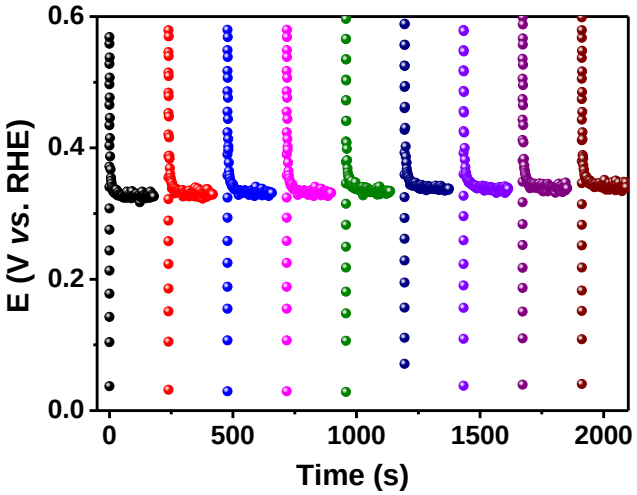

Fig. S11. Sequential chronopotentiometry measurements for NiCu-MoS_2 at 100 mA cm^{-2} for 3 minutes of work and 1 minute on rest in H_2S saturated 1 M NaOH electrolyte, CE: graphite rod, RE: Hg/HgO/1 M NaOH.

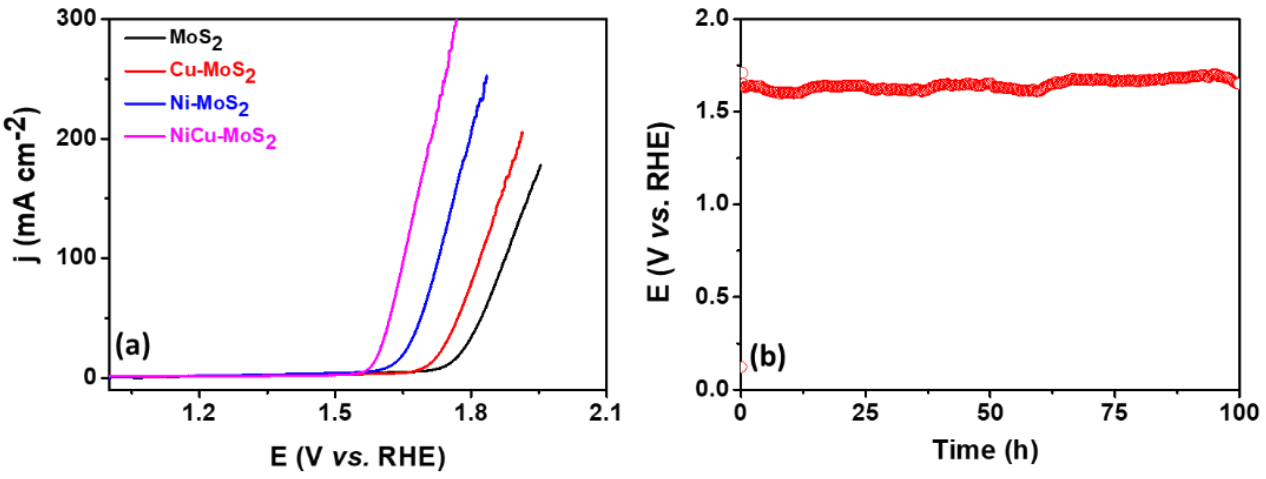

Fig. S12. Linear sweep voltammograms of various catalysts demonstrating OER activity at a scan rate of 5 mV s^{-1}, (b) Chronopotentiometry stability measurements for NiCu-MoS_2 for 100 h at 75 mA cm^{-2} in 1 M NaOH electrolyte, CE: graphite rod, RE: Hg/HgO/1 M NaOH.

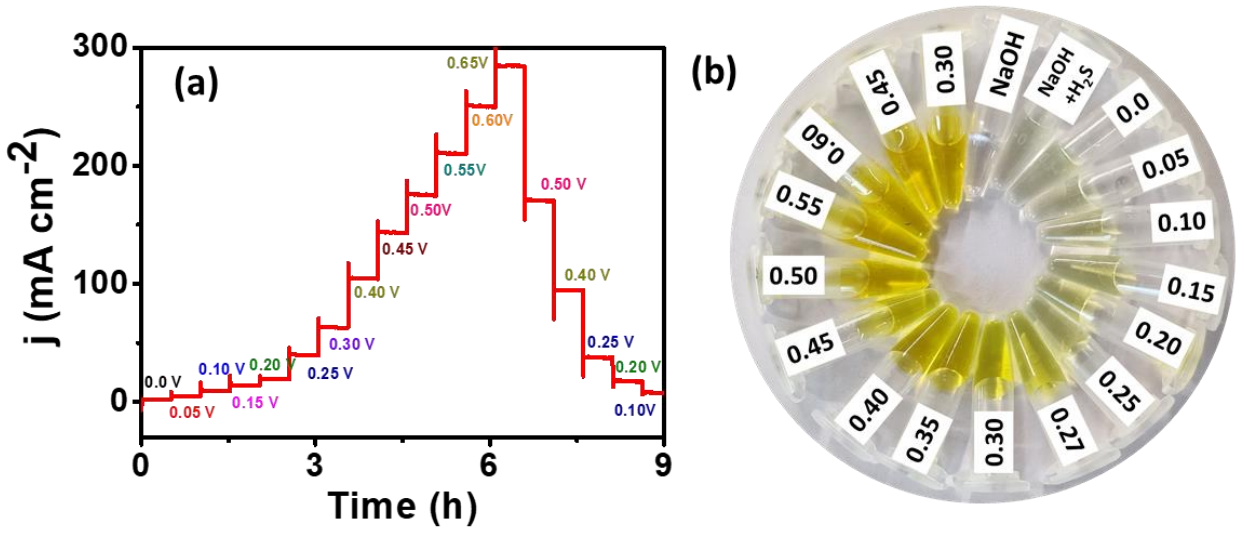

Fig. S13 (a) Chronoamperometric measurement of NiCu-MoS_2 at different applied potentials, (b) photographic images of electrolyte captured during sequential chronoamperometric measurements in H_2S saturated 1 M NaOH by replacing the electrolyte after every 30 h. CE: graphite rod, RE: Hg/HgO/1 M NaOH.

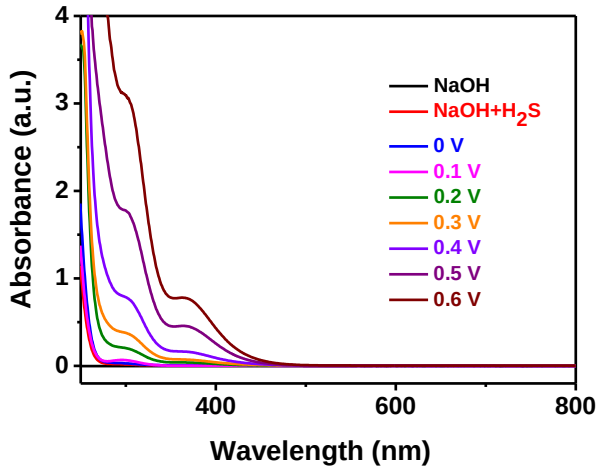

Fig. S14. In-situ UV-Vis spectra of the electrolyte at various potentials during the sequential chronoamperometric study.

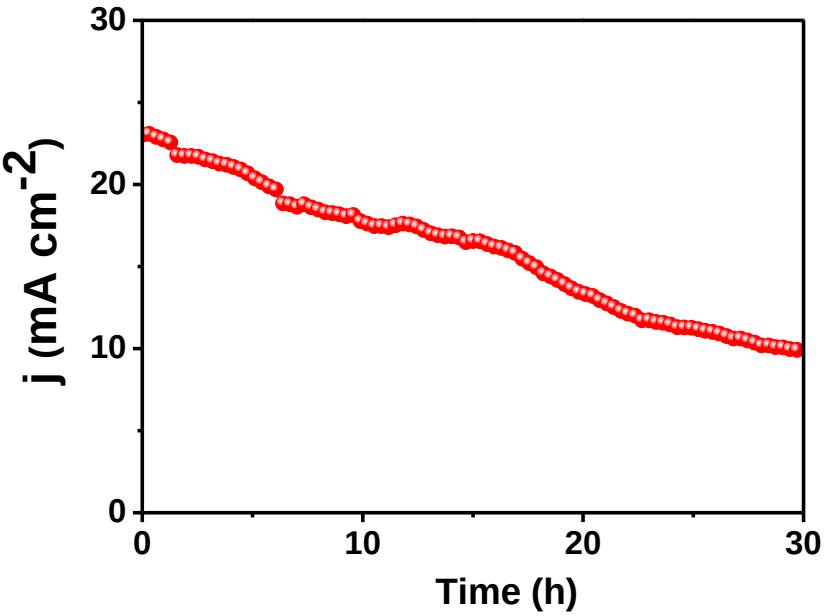

Fig. S15. Chronoamperometry stability measurements for Pt/C for 30 h respectively at 0.4 V *vs.* RHE in H_2S saturated 1 M NaOH, CE: graphite rod, RE: Hg/HgO/1 M NaOH.

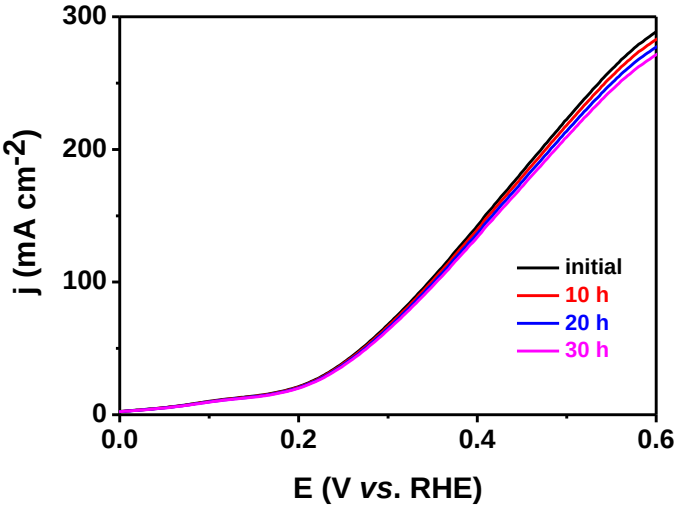

Fig. S16. LSVs for NiCu-MoS_2 at 5 mV s^{-1} after different time intervals during stability test at 0.3 V *vs.* RHE for 30 h.

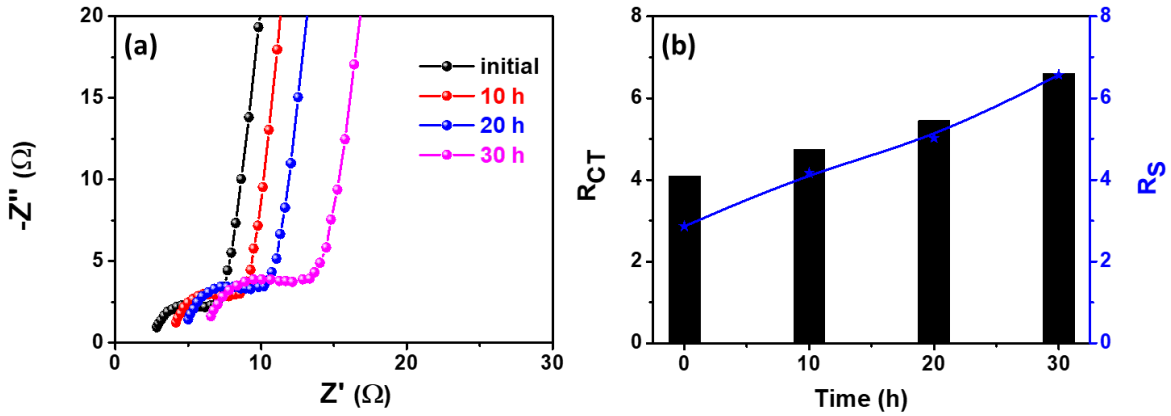

Fig. S17. (a) EIS of NiCu-MoS_2 and (b) corresponding solution resistance and charge transfer resistance measured at different time intervals during the chronoamperometric stability test in H_2S saturated 1 M NaOH electrolyte, CE: graphite rod RE: Hg/HgO/1 M NaOH.

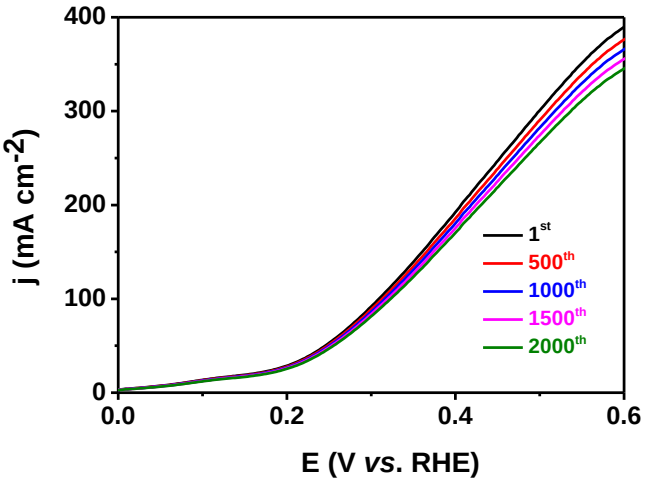

Fig. S18. LSVs of NiCu-MoS_2 during cycling stability at a scan rate of 50 mV s^{-1} over 2000 cycles in H_2S saturated 1 M NaOH electrolyte, CE: graphite rod RE: Hg/HgO/1 M NaOH.

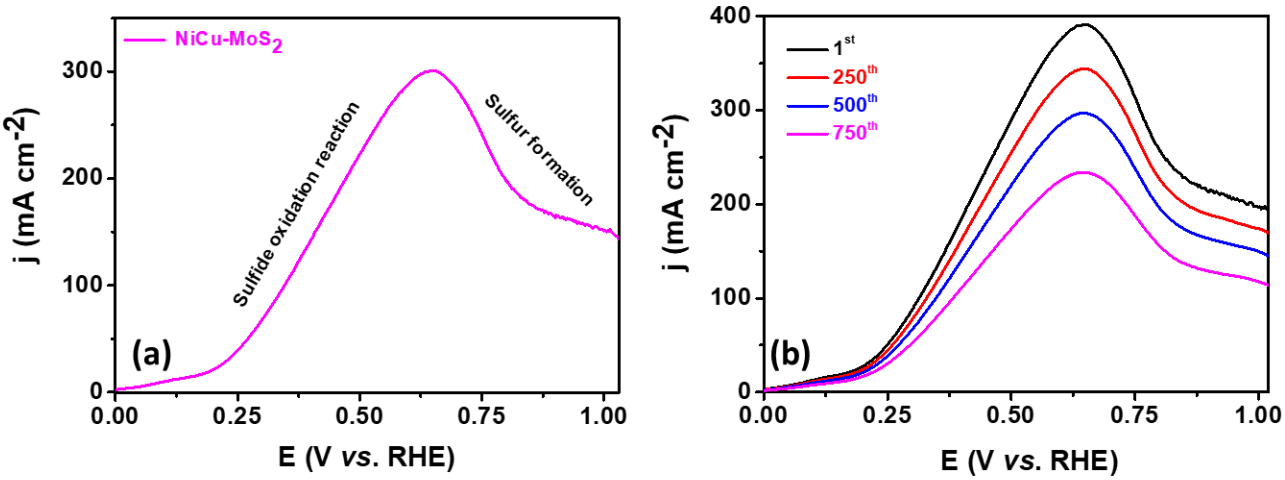

Fig. S19. LSV showing direct sulfur formation, (b) LSVs of NiCu-MoS_2 during cycling stability at a scan rate of 50 mV s^{-1} over 750 cycles during direct sulfur formation in H_2S saturated 1 M NaOH electrolyte CE: graphite rod RE: Hg/HgO/1 M NaOH.

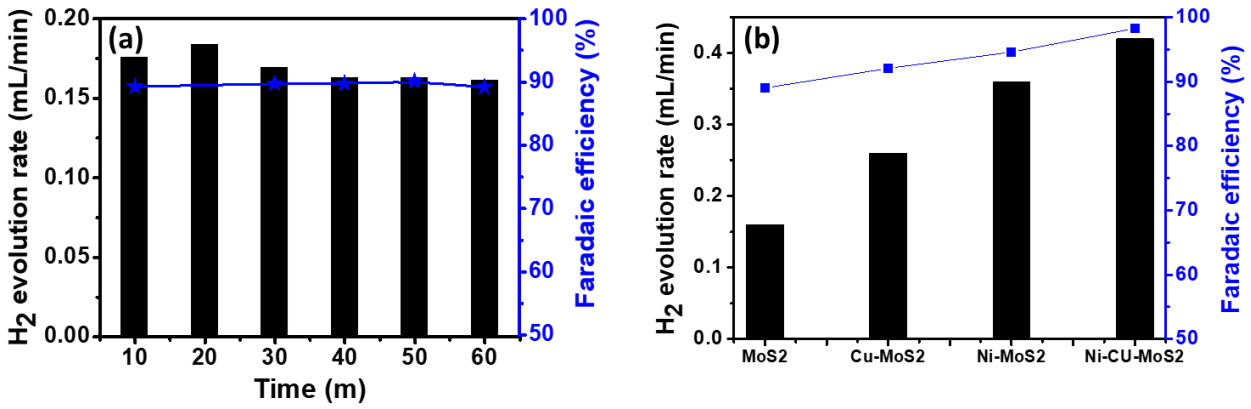

Fig. S20. Bar diagram representing the faradaic efficiency and hydrogen evolution rate for (a) MoS_2 during the stability study @ 0.4 V, (b) for various catalysts @ 0.4 V in H_2S saturated 1 M NaOH electrolyte, CE: graphite rod, RE: Hg/HgO/1 M NaOH.

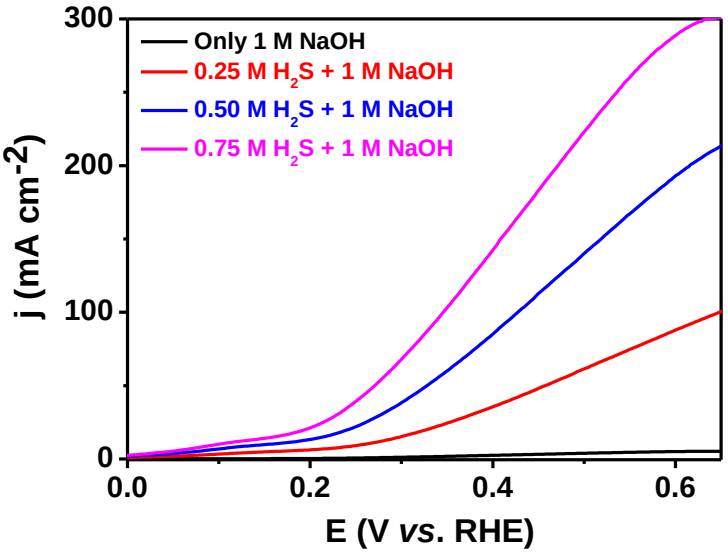

Fig. S21. LSVs for NiCu-MoS_2 at 5 mV s^{-1} without H_2S and with different concentrations of H_2S in 1 M NaOH, CE: graphite rod, RE: Hg/HgO/1 M NaOH.

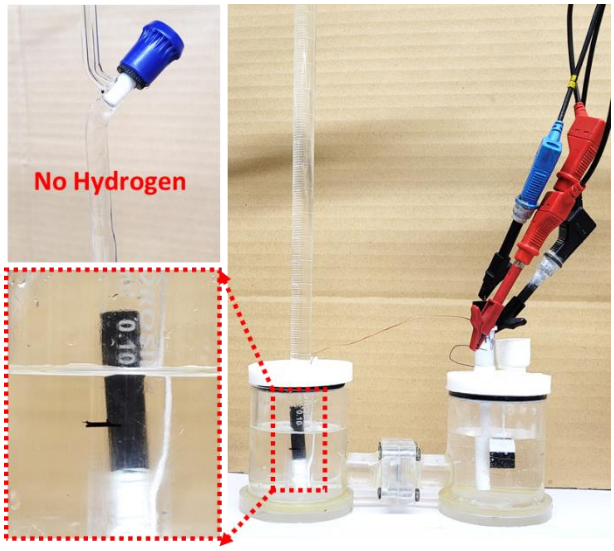

Fig. S22. (a) Photographs of the setup used to quantify H_2 produced during water oxidation by eudiometric method, (b) showing filling of the gas in the burette by displacement of electrolyte.

During autooxidation, cycled electrolyte after the stability study was exposed to atmospheric air. After 10 h of standing, the electrolyte solution becomes colorless. The reaction follows below mentioned equation.

$$S_x^{2-} + O_2 \longrightarrow S_2O_3^{2-} + S$$

These results are consistent with the literature reports. After two days, yellow color S powder started to appear, and after 7 days, we took out the S powder and analyzed it with XRD. Then 5 g of obtained S powder sulfur was added to 50 ml of toluene and heated @ 90 °C for two hours until all the S get dissolved entirely. Afterward, cooling the mixture at room temperature yield S crystal with a needle-like shape.

Table S3: pH of the anolyte and catholyte during the electrolysis.

Time	Anolyte	Catholyte
0	10.4	13.78
10	10.0	13.81
20	9.3	13.93
30	8.7	13.99

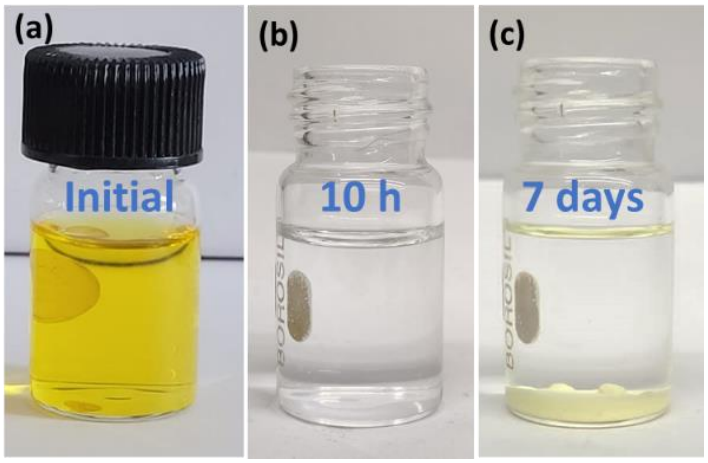

Fig. S23. Photographs of the electrolyte (a) before, (b) after 10 h, and (c) 7 days of autoxidation.

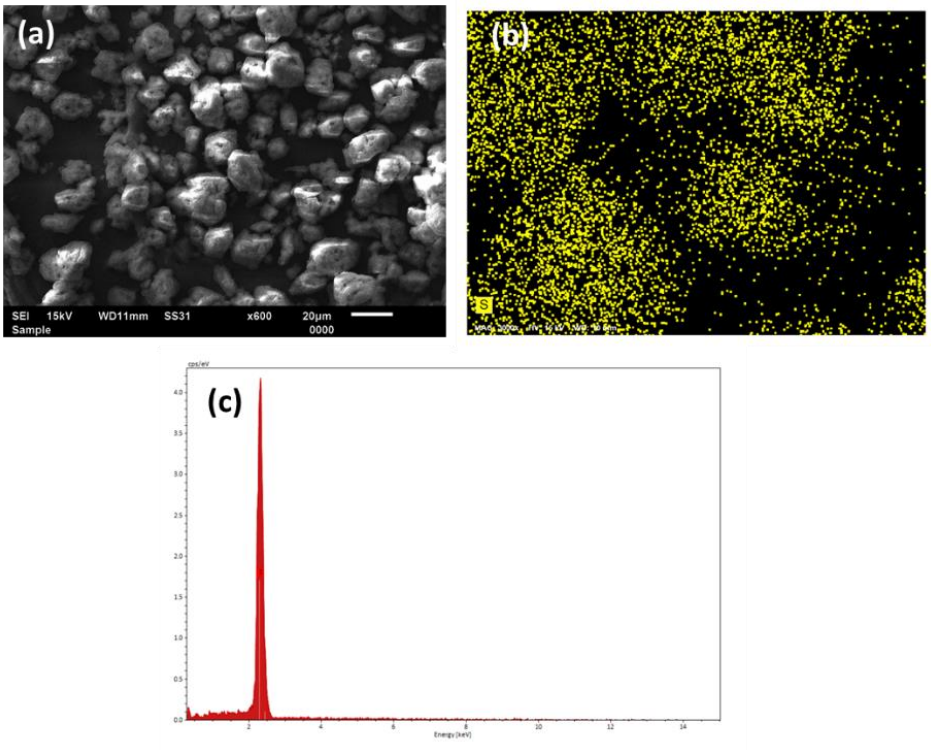

Fig. S24. (a) SEM image, (b) elemental dot mapping image, (c) EDS spectra of the elemental sulfur collected from polysulfide solution after acid treatment.

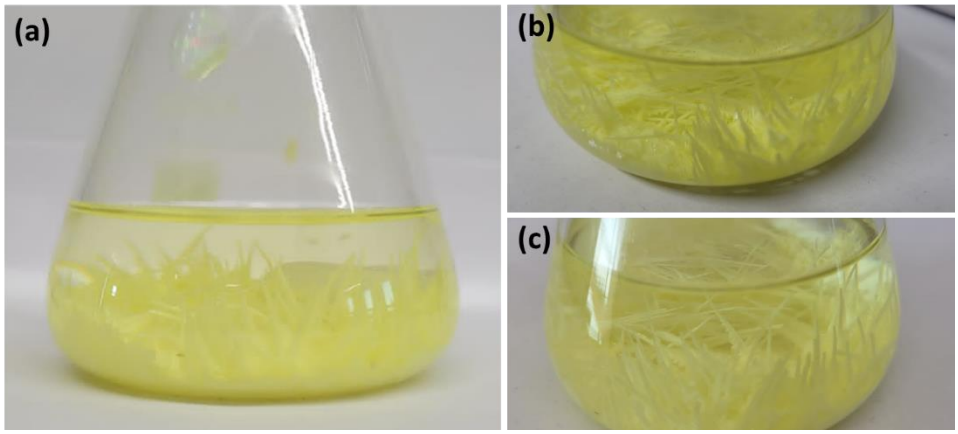

Fig. S25. (a), (b) and (c) are the photographs of crystal Sulfur.

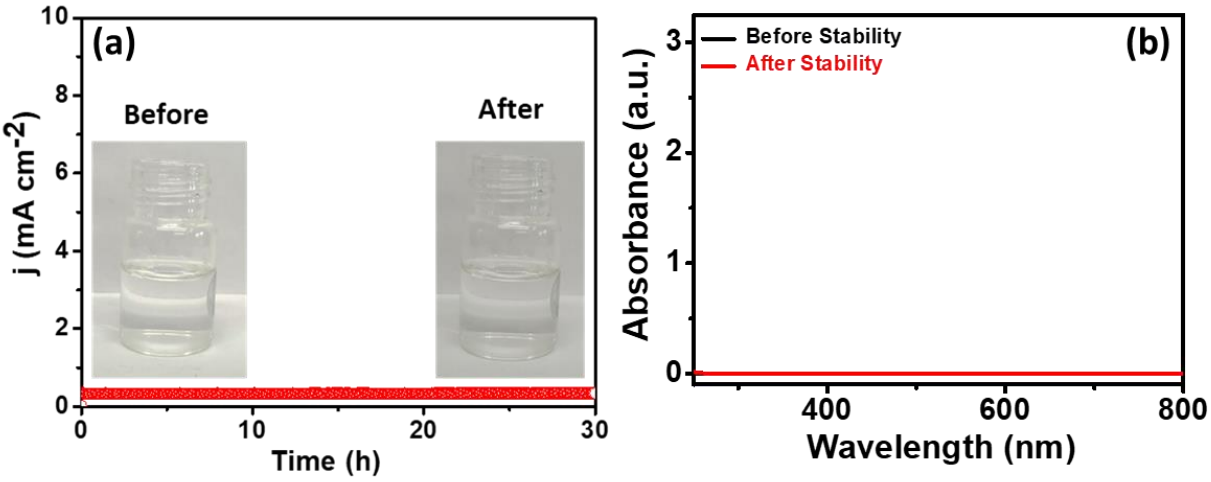

Fig. S26. Chronoamperometric measurement for NiCu-MoS_2 @ 0.5 V *vs.* RHE (Inset images of the electrolyte before and after stability), (b) corresponding UV-vis spectra of the electrolyte.

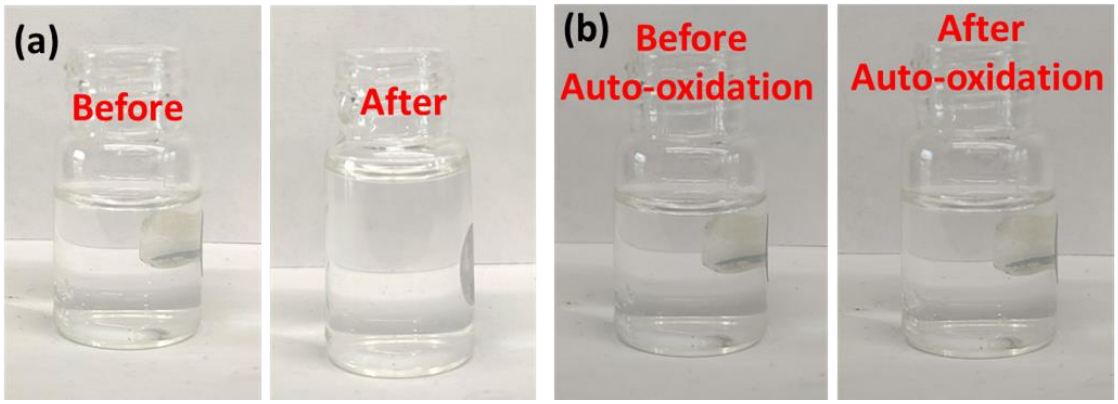

Fig. 27. Photographic images of the electrolyte (a) before and after acid treatment, (b) before after auto-oxidation.

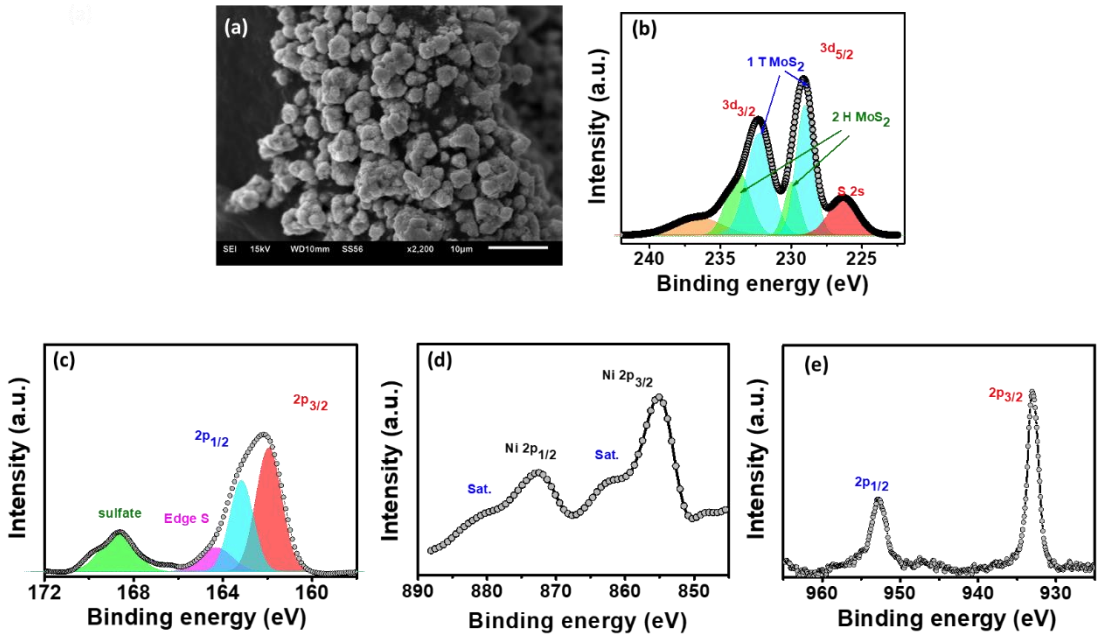

Fig. S28. (a) SEM image, deconvoluted XP spectra of (b) Mo 3d, (c) S 2p, (d) Ni 2p, and (e) Cu 2p of NiCu-MoS_2.

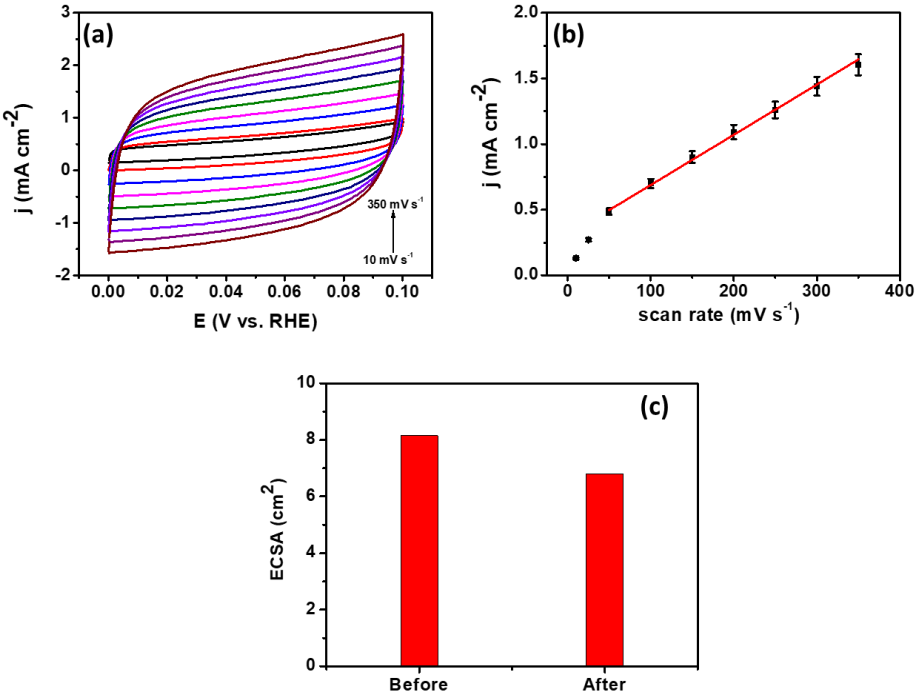

Fig. S29. Cyclic voltammograms of (a) NiCu-MoS_2 after stability test at various scan rates in the non-faradaic potential region (b) corresponding average current versus scan rate plot (c) ECSA before and after the stability test in H_2S saturated 1 M NaOH, CE: graphite rod, RE: Hg/HgO/1 M NaOH.

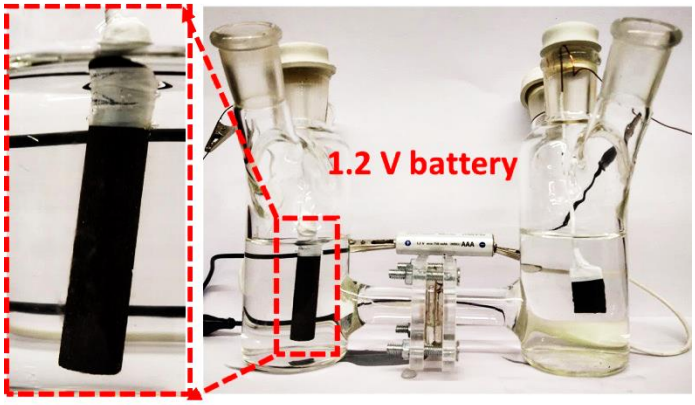

Fig. S30. Photograph of a device with 1.2 V commercial battery unable to carry out water splitting in 1 M NaOH and enlargement in the red block showing the image of the counter electrode.

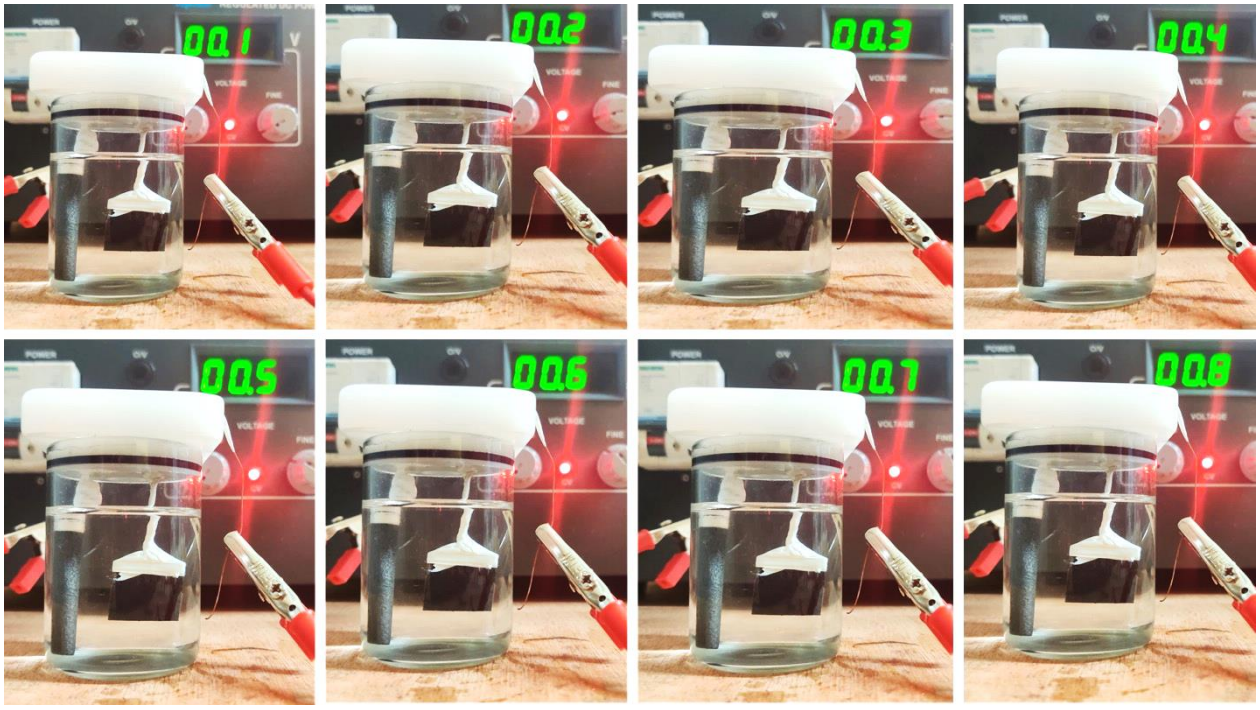

Fig. S31. Photographic images of the device constructed in the undividable cell to drive splitting of H_2O in 1 M NaOH at different potentials, using NiCu-MoS_2 coated graphite paper working electrode and graphite counter electrode.

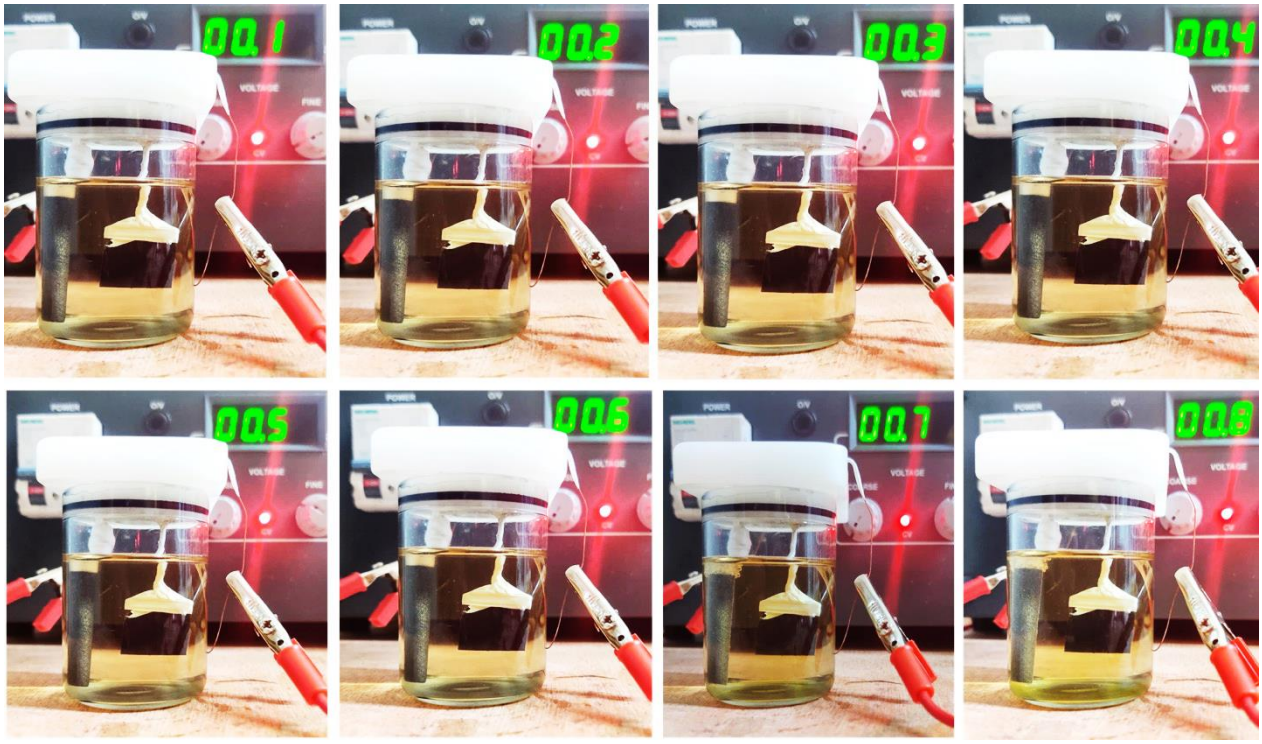

Fig. S32. Photographic images of the device constructed in the undividable cell to drive splitting of H_2S in H_2S saturated 1 M NaOH electrolyte at different potentials, using NiCu-MoS_2 coated graphite paper working electrode and graphite counter electrode.

Fig. S33. Photographic images of the device constructed in H cell to drive splitting of H_2O in 1 M NaOH at different potentials, using NiCu-MoS_2 coated graphite paper working electrode and graphite counter electrode.

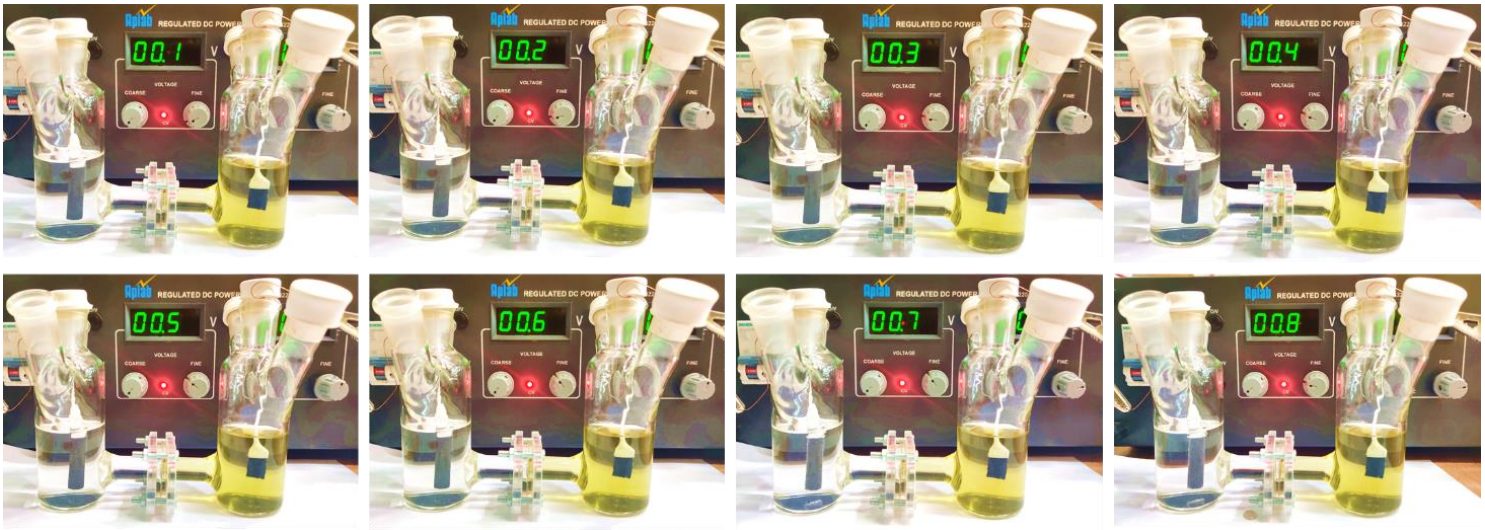

Fig. S34. Photographic images of the device constructed in H cell to drive splitting of H_2S in H_2S saturated 1 M NaOH electrolyte at different potentials, using NiCu-MoS_2 coated graphite paper working electrode and graphite counter electrode.

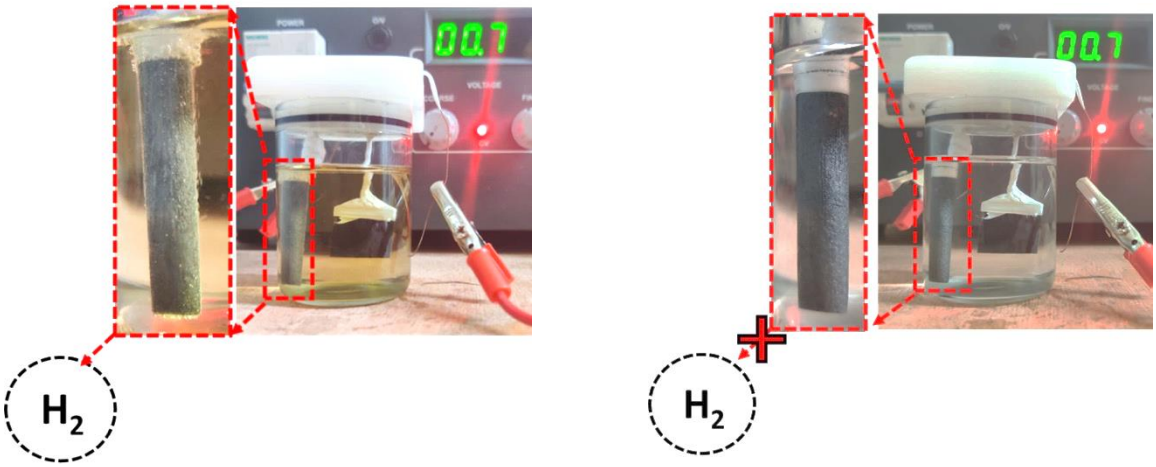

Fig. S35. Photographs of a device constructed to drive electrochemical splitting of H_2S (left) in H_2S saturated 1 M NaOH and H_2O (right) in 1 M NaOH at 0.7 V direct potential using NiCu-MoS_2 coated graphite paper working electrode and graphite counter electrode.

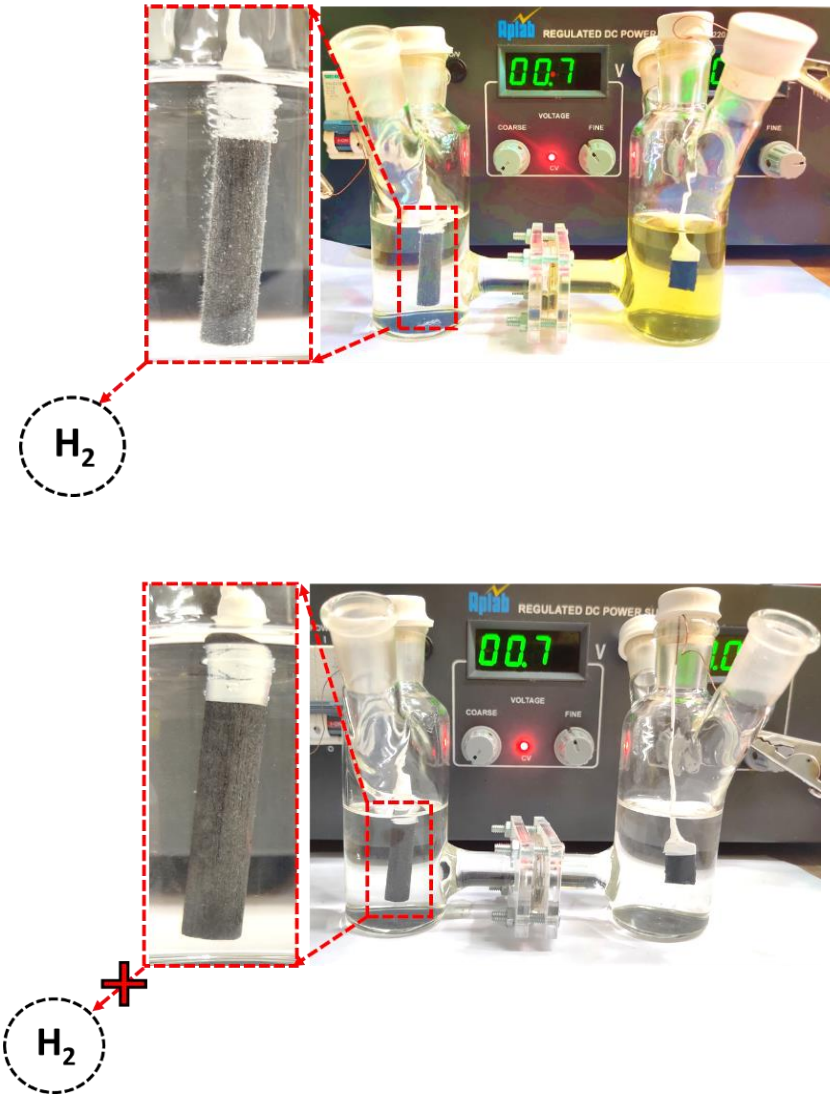

Fig. S36. Photographs of a device constructed to drive electrochemical splitting of H_2S (top) in H_2S saturated 1 M NaOH and H_2O (bottom) in 1 M NaOH at 0.7 V direct potential using NiCu-MoS_2 coated graphite paper working electrode and graphite counter electrode.

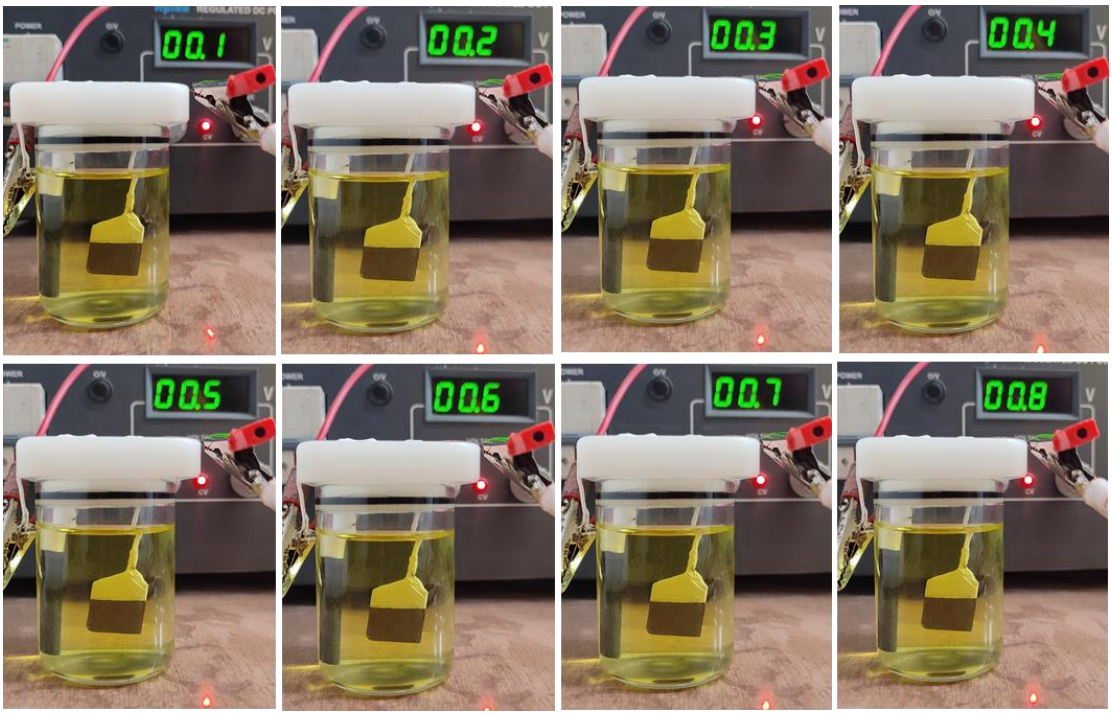

Fig. S37. Photographic images of the device constructed in the undividable cell to drive splitting of H_2S in H_2S saturated 1 M NaOH electrolyte at different potentials, using bare carbon paper as WE and graphite rod as a counter electrode.

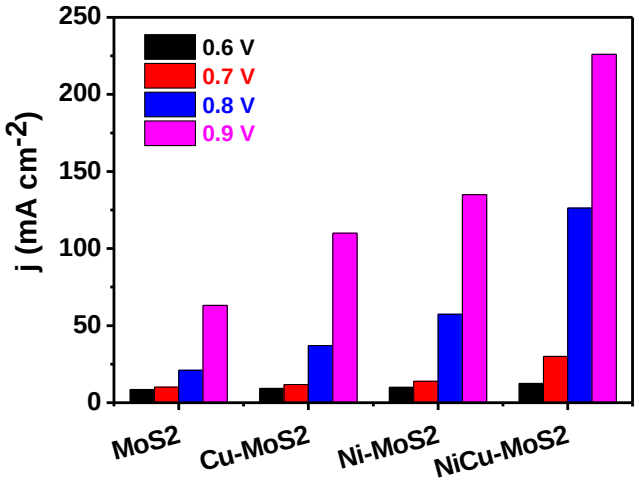

Fig. S38. Bar diagram representing current densities obtained for various catalysts at different potentials for overall H_2S splitting in H_2S saturated 1 M NaOH electrolyte at a scan rate of 5 mV s^{-1}, WE: NiCu-MoS_2, CE: NiCu-MoS_2.

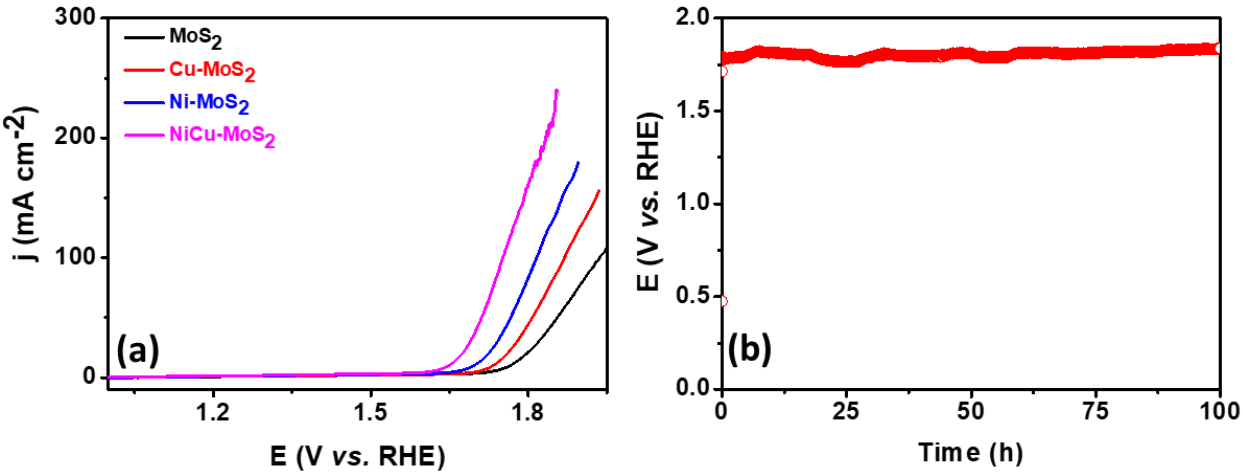

Fig. S39. Linear sweep voltammograms of various catalysts demonstrating overall water electrolysis at a scan rate of 5 mV s^{-1}, (b) Chronopotentiometry stability measurements for NiCu-MoS_2 for 100 h at 75 mA cm^{-2} in 1 M NaOH electrolyte, WE: NiCu-MoS_2, CE: NiCu-MoS_2.

Table S4: Comparison of obtained current density for NiCu-MoS_2 towards SOR with reported literature.

Catalyst	Current density (mA cm^{-2})		References
	0.3 V	0.4 V	
Raney Ni	0.50	1.39	2
IrO_2	1.80	6.57	3
40% Pt/C	3.31	14.73	4
CoNi@NGs	4.09	26.55	4
MoS_2	0.48	0.70	5
$CoFeS_2$(3:1)	50	122	6
NiCu-MoS_2	75	144	This Work

References:

1. N. Thakur, M. Kumar, S. D. Adhikary, D. Mandal and T. C. Nagaiah, *Chem. Commun.*, 2019, **55**, 5021-5024.
2. K. Petrov and S. Srinivasan, *Int. J. Hydrogen Energy*, 1996, **21**, 163-169.
3. B. Miller and A. Chen, *Electrochim. Acta*, 2005, **50**, 2203-2212.
4. M. Zhang, J. Guan, Y. Tu, S. Chen, Y. Wang, S. Wang, L. Yu, C. Ma, D. Deng and X. Bao, *Energy Environ. Sci.*, 2020, **13**, 119-126.
5. A. E. Sanlı, A. Aytaç and M. Mat, *Int. J. Hydrogen Energy*, 2014, **39**, 9221-9229.
6. M. Kumar and T. C. Nagaiah, *J. Mater. Chem. A*, 2022, DOI: 10.1039/D1TA09888H.